

# ***Ab initio* investigations of dioctahedral interlayer-deficient mica: modelling 1M polymorphs of illite found within gas shale**

DAWN L. GEATCHES\* and JENNIFER WILCOX

Energy Resources Engineering, 367 Panama Street, Stanford, CA 94305–2220, USA

\*Corresponding author, e-mail: geatches@stanford.edu

**Abstract:** In this investigation we create a variety of dioctahedral, interlayer (cation)-deficient mica clay mineral models of the 1M-illite series, using the *ab initio* method of density functional theory (DFT), employing plane waves, pseudo potentials, and super cells. The structures we create are modelled on an average formula of illite such as  $(\text{Ca}_{0.059}, \text{K}_{0.655})(\text{Si}_{3.597}, \text{Al}_{0.403})(\text{Fe}_{0.628}, \text{Al}_{0.969}, \text{Mg}_{0.428})\text{O}_{10}(\text{OH})_2$ , as well as existing crystal structures and experimental data. This study investigates the relative positions of both octahedral and tetrahedral cation substitutions (*e.g.*  $\text{Fe}^{3+}$  for  $\text{Al}^{3+}$  and  $\text{Al}^{3+}$  for  $\text{Si}^{4+}$ ) in both trans- and cis-vacant structures. The purpose of this work is to create robust, representative models of single layers (I) and double layers (I-I) of illite found within gas shale, that can be used in future investigations. We examine lattice parameters, interatomic distances of tetrahedral and octahedral sheets, K–O distances, and K positions, and find reasonable agreement with experimental data, and excellent agreement with simulated data of similar structures. Finally, to enable experimental characterization of samples of illite with different compositions, we provide simulated X-ray powder diffraction (XRPD) patterns including up to the first ten (*h k l*) reflections, and find characteristic identifiers of trans- and cis-vacant micas in agreement with previous theoretical and experimental studies. We conclude that the models we create are feasible models of I and I-I layers of illite found within shale and are ready for use in future work.

**Key-words:** interlayer-deficient mica, 1M-polymorph, illite, shale, DFT, trans-vacant, cis-vacant.

## **1. Introduction**

Within a gas-shale matrix the proportion of clay minerals that belong to the illite series comprises up to 40 % of the total clay mineral content, which constitutes up to 60 % of the overall shale contents. In the Barnett shale, illite is the end product of diagenesis (Liming *et al.*, 2012) and forms on the transformation of smectites (Lausen *et al.*, 1999). The presence of illite provides information about sedimentation and oil generation, because it represents the stage where hydrocarbons have left the smectite interlayers and migrated through to, for example, natural fractures in the minerals of shale. The evidence for this is two-fold, firstly the correlation between the collapse of smectite interlayers with the (assumed) release of its water (Eslinger & Pevear, 1988; Lindgreen, 1991), and secondly, the nature of the formation of shale itself. Lash & Blood (2004) determined that the origin of shale fabric arises from the accumulation of organic-rich mud as clay floccules, probably due to electrostatic and organic cohesive forces, and that these particles were then subject to pressure compaction, resulting in the mature shale fabric. This intimate relationship between organic matter and clay minerals within the mud lends credence to the theory that clay minerals catalyze hydrocarbon-forming reactions (Almon & Johns, 1975;

Eslinger & Pevear, 1988), but even if this is not the case, they potentially serve as hydrocarbon storage space, by virtue of their smectitic/swelling nature. Illitization of smectites leads to mixed layers of smectites and illite (I-S layers) as well as discrete illite (I) with a ratio in the Barnett shale of I-S:I of 4:1, where the I-S layers have an expandability of 15 % (Day-Stirrat *et al.*, 2008). This indicates the possibility of  $\text{CH}_4$  retained within the I-S composite layers of gas shale, and also suggests that, on its exit, the layers could be occupied by  $\text{CO}_2$ . This is potentially promising for long-term  $\text{CO}_2$  storage as one of the proposed methods of off-setting the increase in atmospheric  $\text{CO}_2$  is to store it in depleted gas-shale reservoirs (Wilcox, 2012). However, to study interactions occurring between illite and its environment, robust, atomistic models are required, from which surfaces (of interaction) can be created. This study focusses on creating such models.

Illite is classed as a “...dioctahedral interlayer-deficient mica..” (Fleet, 2003) characterized by non-swelling behaviour and an interlayer dominated by K ions. Each layer consists of tetrahedral-octahedral-tetrahedral (TOT) sheets composed of (mainly)  $\text{T}_2^{4+}\text{O}_5$  and  $\text{R}_2^{3+}\text{O}_5$ , respectively, where T is usually Si and R is predominantly Al. Substitutions of the T-cations by  $\text{Al}^{3+}$  and O-cations by  $\text{Fe}^{2+}/\text{Fe}^{3+}$  and  $\text{Mg}^{2+}$  produces a negatively charged TOT

layer. The negative charge is then balanced by positive interlayer cations, which, in the case of illite, are mainly  $K^+$ , (well documented)  $NH_4^+$  (Lindgreen *et al.*, 1991a and b), and  $H_3O^+$  (Nieto *et al.*, 2010). The average formula for K-interlayer illite is  $(Ca_{0.059}, K_{0.655})(Si_{3.597}, Al_{0.403})(Fe_{0.628}, Al_{0.969}, Mg_{0.428})$  per  $O_{10} (OH)_2$ . The octahedral-layer cations fill two of three possible octahedral sites, hence the description dioctahedral. There are two types of occupation of these octahedral sites (M1 and M2), and conversely, they are identified by their vacancies and the positions of the hydroxyl groups around the vacant site. Where pairs of hydroxyl groups lie on opposite apices of the vacant cation site this is “trans-vacant”, and where the pairs lie on the same side of the vacant cation site this is “cis-vacant”. Further explanation can be found in Meunier (2005).

Within the mica group, there are six polymorphs formed by the various stacking possibilities of the TOT layers with each other, *i.e.*, the TOT sheets are all translated or rotated to the same degree, but relative to another TOT layer could be variously translated or rotated (Nespolo, 2001). Fortunately, there is experimental data concerning the polymorphs of illite within shale, reporting that it occurs as two main polytypes,  $1M$  and  $2M_1$  (Drits & Zviagina, 2009). The work we present here focuses on the creation, from first principles, of varieties and structures of  $1M$ -illite found within a gas-shale environment ( $2M_1$  structures form the subject of a second study). There are currently few other such DFT investigations into the illite series of micas, although there are DFT studies into the cation arrangement in dioctahedral phyllosilicates (Hernández-Laguna *et al.*, 2006; Escamilla-Roa *et al.*, 2013), containing comparative results, as the variety of  $1M$ -illite structures we create are also dioctahedral phyllosilicates. The aim of our work is to create accurate illite structures that are representative of physical samples of illite within gas shale, which includes single and double layers or “sandwiches”. These represent the “I” and “I-I” in mixed illite-smectite stacks, respectively. To enable non-DFT specialists to create their own atomistic illite models or more generally, those of other clay minerals of the dioctahedral phyllosilicate classification, further details (as highlighted in the text) are freely available online as Supplementary Material linked to this article (<http://eurjmin.geoscienceworld.org>).

## 2. Models

As previously mentioned,  $1M$ -illite exists as both cis-vacant (cv) and trans-vacant (tv), although the latter is more widely reported in the literature (Sainz-Diaz *et al.*, 2001; Bergaya *et al.*, 2006; Drits & Zviagina, 2009), which could be because it is hypothesised to be one of the conformations created at the end of the illitization process. Ylagan *et al.* (2000) say that the illite-smectite transformation progresses through cv smectites to cv/tv and  $1M_d$  I-S to tv and  $1M$ -illite, and finally to  $2M_1$ -illite. They also report that variations in the shape of illite crystals, such as plates and laths, correspond to different polytypic combinations of cv and tv layers. For the purposes of investigating  $1M$ -illite within shale, the following are of most interest:  $1M$ -cv and  $1M$ -tv plus a mixed model of cv/tv. Figure 1 illustrates the differences in the location of the hydroxyl groups around the vacancy in the dioctahedral, 2:1, trans- and cis- vacant illite models in this study.

According to analysis of physical illite samples by Lindgreen (1991), illitization of smectites produces ordering of I-S layers randomly, in I-S or in I-S-I formations, which means that illite layers occur in an illitized stack either individually or as I-I neighbours. Therefore, it is necessary to create both single (I) and double (I-I) layers of illite models to represent illite layers found in gas shale.

Throughout this manuscript several terms are used to describe the various models, for example, “I”, “single layer”, “unit cell” are all synonymous, as are “I-I”, “double layer” and “sandwiches”. In an effort to avoid overwhelming the reader with a multitude of labels we have kept these to a minimum and grouped models together in Sections. Also, we do not refer to every permutation we created, but distinguish between them where their differences are relevant.

### 2.1. Single-layer/unit-cell models

#### 2.1.1. $1M$ -tv

The initial, parent structure of general formula  $(KAl_4(Si_7Al)O_{20}(OH)_4)$  for all  $1M$ -tv unit cells was obtained from Drits *et al.* (2010). To accommodate both the average formula  $(K_{1.43}(Si_{6.90}, Al_{1.10})(Fe_{0.40}, Al_{3.27}, Mg_{0.33}))$  and efficient computation, we made three distinct varieties of  $1M$ -tv structures. All three varieties contain a

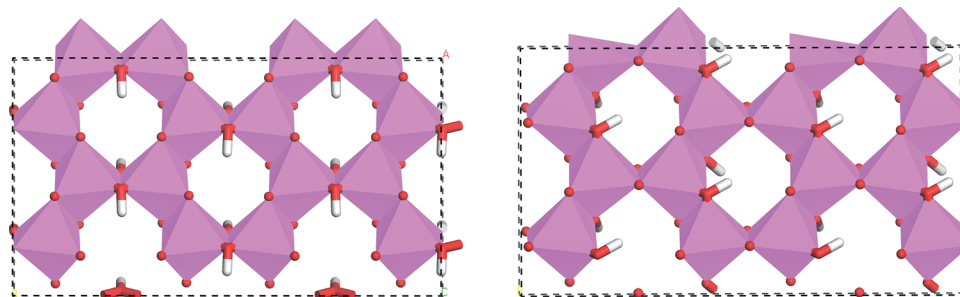


Fig. 1. Trans- (left) and cis-vacant (right) octahedral sheet configurations for  $1M$ -illite.

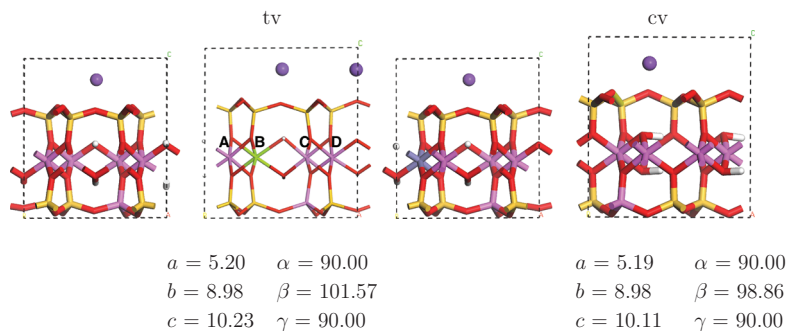


Fig. 2. Single unit cells and their initial lattice parameters of 1M-tv, (left column – from left to right, Al-, Mg- and Fe-illite), 1M-cv Al-illite all before relaxation. A-D are possible positions of the Mg (and Fe) substitution in the octahedral sheet. Shown are substitutions of Mg in position B and Fe in position A. Colour scheme used throughout this study: oxygen – red; hydrogen – white; aluminium – pink; silicon – yellow; magnesium – green; iron – grey-blue; potassium – purple. The dashed line is the periodic boundary of a unit cell. Lengths (to 2 decimal places) are in Å and angles in degrees, throughout this study.

substituted Si for Al in the tetrahedral sheet, and either an Fe, Mg or Al (*i.e.* no cation substitution of Al) in the octahedral sheet (see Fig. 2). These three different varieties are labelled Fe1Mtv ( $\text{K}(\text{Si}_7\text{Al})\text{FeAl}_3\text{O}_{20}(\text{OH})_4$ ); Mg1Mtv ( $\text{K}_2(\text{Si}_7\text{Al})\text{MgAl}_3\text{O}_{20}(\text{OH})_4$ ), and Al1Mtv ( $\text{K}(\text{Si}_7\text{Al})\text{Al}_4\text{O}_{20}(\text{OH})_4$ ), respectively.

Al1Mtv contains only one substitution of Al for Si in a tetrahedral sheet, and its position is identical to that of any other Al-for-Si substitution, consequently only one model of Al1Mtv was required. The sole substitution of  $\text{Al}^{3+}$  for  $\text{Si}^{4+}$  giving a layer charge of  $-1$  requires only one charge-balancing  $\text{K}^+$  ion. For Mg1Mtv, a Mg-for-Al in the octahedral sheet plus an Al-for-Si substitution in a tetrahedral sheet yields four different relative positions of the substitutions to consider: *e.g.* Mg and Al directly in-line; Mg to the left of Al; Mg to the right of Al; Mg two positions to the right of Al. The substitution of  $\text{Al}^{3+}$  for  $\text{Si}^{4+}$  and  $\text{Mg}^{2+}$  for  $\text{Al}^{3+}$  yields an overall layer charge of  $-2$ , requiring two  $\text{K}^+$  ions to balance the charge. For Fe1Mtv, the number of Fe to Al permutations is the same as for Mg1Mtv, and the Fe in the octahedral sheet is assumed to be  $\text{Fe}^{3+}$ . Substitution of  $\text{Fe}^{3+}$  for  $\text{Al}^{3+}$ , and  $\text{Al}^{3+}$  for  $\text{Si}^{4+}$  in a tetrahedral sheet gives an overall layer charge of  $-1$  and so, Fe1Mtv requires only one charge-balancing  $\text{K}^+$  ion.

### 2.1.2. 1M-cv

1M-cv develops or grows in Fe- and Mg-poor and Al-rich environments (Drits *et al.*, 2006), suggesting that for this study, an all-Al model (Al1Mcv) would be sufficient. The coordinates used for the single-layer, 1M-cv model can be found in Drits *et al.* (2006); this model contains an all-Al octahedral sheet and a single, Al-for-Si substitution in the tetrahedral sheet (Fig. 2), requiring only one charge-balancing K ion. Similar to the Al-tv type, the position of the Al-for-Si substitution is identically isomorphic, hence only one model was required.

## 2.2. Double-layer/“sandwich” models

### 2.2.1. 1M-tv

To create an I-I double-layer, or “sandwich” within the context of this fragment occurring within an illitized stack of the clay portion of shale, we sandwiched together two of the single unit cells, such that each layer shares two interlayer K ions. For the 1M-polymorphs, adjacent layers are not rotated with respect to one another, hence we placed the upper layer above the lower without any rotation. For an all-Al I-I sandwich, this required an Al-for-Si substitution in a tetrahedral sheet of each layer, which we have chosen to be in the outer sheets of the I-I layers, because this is potentially the site of chemical reactivity, an area we will investigate in future studies. These substitutions resulted in four possible permutations of their relative positions, the same as those described in Section 2.1.1. Figure 3 shows examples of the Al-, Fe- and Mg- sandwiches and the positions of the possible cation substitutions.

When creating sandwiches of Mg1Mtv and Fe1Mtv, we chose to conjoin one layer of Al1Mtv with one layer of Mg1Mtv, and separately Fe1Mtv, to comply with the proportions in the average formula. There were three substitutions in the sandwich of Fe1Mtv (two Al-for-Si substitutions in tetrahedral sheets and one  $\text{Fe}^{3+}$ -for- $\text{Al}^{3+}$  in the octahedral sheet) creating sixteen possible permutations of relative, substituted-cation positions. For Mg1Mtv there were two substitutions, one Al-for-Si in a tetrahedral sheet of an Al-layer, and one  $\text{Mg}^{2+}$ -for- $\text{Al}^{3+}$  in the octahedral sheet of the Mg-layer, creating four possible permutations of the relative cation positions.

### 2.2.2. 1M-cv

Two unrelaxed unit cells of 1M-cv, Al1Mcv were joined together with two interlayer K ions, each cv layer having one Al-for-Si substitution in a tetrahedral sheet, giving four possible permutations of the relative cation positions (Fig. 3).

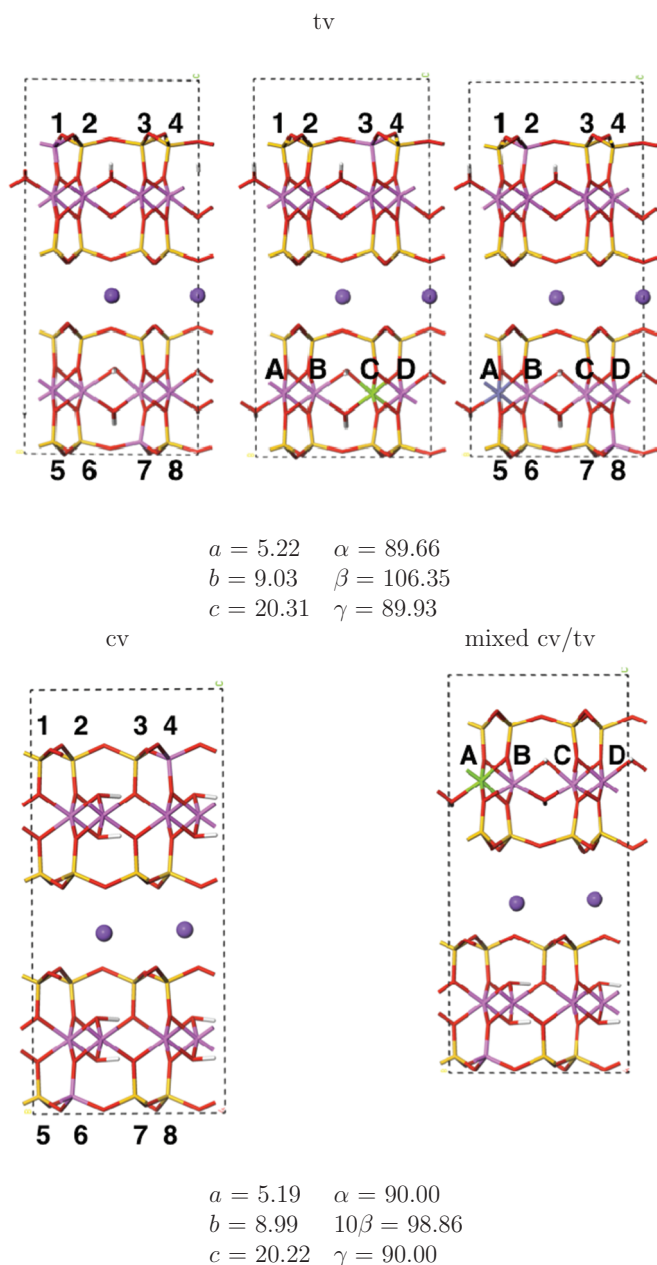


Fig. 3. Double layer cells or “sandwiches” of 1M-types before relaxation. A-D denote possible octahedral site substitutions of Fe and Mg, and 1–8 denote possible tetrahedral site substitutions of Al. Lattice parameters for all 1M-tv sandwich models were identical before relaxation; similarly, 1M-cv, Al-illite and mixed cv/tv, Al/Mg-illite shared identical, initial lattice parameters.

### 2.2.3. Mixed cv/tv

The mixed-layer model comprises a single layer of Al1Mcv plus a layer of Mg1Mtv to form a mixed (cv/tv) two-layer “sandwich”. The Al1Mcv layer has an Al-for-Si substitution in a tetrahedral sheet and the Mg1Mtv layer a Mg-for-Al substitution in its octahedral sheet, requiring in total two K ions to balance the total charge. The relative cation positions produced four permutations. A sandwich cell of Al/Mg1Mcv/tv is shown in Fig. 3.

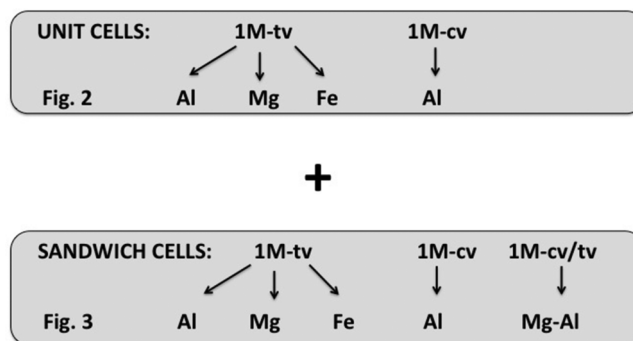


Fig. 4. Schematic summarizing the models made and their corresponding figures.

For ease of reference, the variety of models from single to sandwiches together with the different cation substitutions and the different polytypes is summarized in Fig. 4.

### 2.3. Average formula

The average formula of illite is  $K_{1.43}(Si_{6.90}, Al_{1.10})(Fe_{0.40}, Al_{3.27}, Mg_{0.33})$  per  $O_{20}(OH)_4$  (Drits & Zviagina, 2009), which contains Fe and Mg in the octahedral sheets; DFT is a computationally expensive method making it prudent to create the smallest possible representative model. Incorporating both Fe and Mg in the same octahedral sheet would create too high a ratio for small models (see Table 1), and doubling the size of the model would increase the computational time. This conundrum was reconciled by creating three different sandwich structures of illite, incorporating Fe and Mg (separately) into the octahedral sheet plus an all-Al octahedral sheet. In this way, we were able to approximate the average formula without too high an Fe and Mg octahedral cation count.

Table 1 compares the number of cations per unit of  $O_{20}(OH)_4$  in all models in this study, together with some formulae gained from experimental analysis of samples. There are several points to note regarding the cation counts, namely: the experimental formulae vary in proportions for all cations; the number of K ions is lower in all theoretical models (except unit cell, tv, Mg-) than the experimental formulae; the theoretical number of Si and Al ions in the tetrahedral sheet is mostly higher and lower, respectively, than the cited data; the cv, Al- unit cells and the tv, sandwich models are closest to their “average” cited formulae; the deficit (when compared to the cited data) of tetrahedrally-substituted Al in cv, sandwich Al-models matches the deficit in  $K^+$ .

From these observations we can say that given the size of our models and the crystallographic data we have used as templates, the range of models we have created is a reasonable first attempt at producing a variety of structures encompassed by the term “1M-illite series”. The outstanding deficiency is the number of K ions in our theoretical models, but increasing this number would necessitate an increase in the number of Al-substitutions in the

Table 1. Number of atoms for all types of models in this study and cited experimental data calculated per  $\text{O}_{20}(\text{OH})_4$ . “T-” and “O-” are tetrahedral and octahedral respectively. Fe is  $\text{Fe}^{3+}$  plus  $\text{Fe}^{2+}$  for the general formula and references, where the proportion of  $\text{Fe}^{2+}$  is usually lower than that of  $\text{Fe}^{3+}$ . Fe is assumed to be  $\text{Fe}^{3+}$  in the atomistic models although its oxidation state cannot be determined until post relaxation. This is discussed further in Section 4.

Model	T-sheet			O-sheet		
	K	Si	Al	Fe	Al	Mg
General formula (Drits & Zviagina, 2009)	1.43	6.9	1.1	0.4	3.27	0.33
Single layer – tv	Al	1	7	1	–	4
	(Hernández-Laguna <i>et al.</i> , 2006) S7	1	7	1	–	4
	(Środón, 1999)	1.44	6.5	1.5	0.18	3.68
	Mg	2	7	1	–	3
	(Sokolova <i>et al.</i> , 1976)	1.72	7.6	0.4	0.52	2.32
Single layer – cv	Fe	1	7	1	1	3
	(Sakharov <i>et al.</i> , 1990)	1.48	6.88	1.12	1.06	2.54
	Al	1	7	1	–	4
	(Escamilla-Roa <i>et al.</i> , 2013) cis2	1	7	1	–	4
	(Zvyagin <i>et al.</i> , 1985)	–	–	–	low	–
Sandwiches – tv	(Drits <i>et al.</i> , 1993)	no data given				
	(Drits <i>et al.</i> , 1995)	1.32	6.8	1.2	0.18	3.5
	(Lee, 1996)	Al-rich illite				
	Al	1	7	1	–	4
	(Środón, 1999)	1.44	6.5	1.5	0.18	3.68
Sandwiches – cv	Mg	1	7.5	0.5	–	3.5
	(Środón, 1999)	1.56	6.9	1.1	0.26	3.14
	Fe	1	7	1	0.5	3.5
	(Sakharov <i>et al.</i> , 1990)	1.48	6.88	1.12	1.06	2.54
	Al	1	7	1	–	4
Mixed -cv/tv	(Drits <i>et al.</i> , 1993)	1.48	6.56	1.44	0.08	3.74
	Mg/Al	1	7.5	0.5	–	3.5
	(Gavrilov & Tsipursky, 1988)	Al-rich illite				

tetrahedral sheet, or an  $\text{Al}^{3+}$  for (generic)  $\text{M}^{2+}$  in the octahedral sheet, and both of these numbers are generally relatively close to their average experimental values as they are. It would be possible to make various substitutions in the sandwich models to attempt to get closer to the experimental proportions, but in our first attempt, we have chosen the simplest route by accepting the  $\text{K}^+$ -interlayer deficit to keep the number of possible permutations and configurations manageable. Given that all Si-O hexagonal rings are occupied by  $\text{K}^+$  in the sandwich models, the  $\text{K}^+$  deficit must be due to a lack of vacancies in the octahedral sheet. Investigating this latter phenomenon is outside the scope of this study.

### 3. Computational details

All calculations were processed with the CASTEP code (Clark *et al.*, 2005), using a planewave basis set within the DFT formalism (Hohenberg & Kohn, 1964; Kohn *et al.*, 1965a and b; Payne *et al.*, 1992). Convergence testing showed that a planewave basis represented by a kinetic energy cut-off of 500 eV gave an energy difference in total energies of less than 0.5 meV per atom for higher cut-offs. The Brillouin-zone integrations were performed on various grids according to the differently sized models, but were all converged to within the error bound just described. We

used the generalized gradient approximation (GGA) exchange-correlation functional, specifically Perdew, Burke and Ernzerhof (PBE) (Perdew *et al.*, 1996), as this describes molecular bonding to a greater accuracy than does the local density approximation (LDA). The PBE ultra-soft pseudopotentials were used as these are consistent with the PBE exchange functional. The (geometry) optimizer was Broyden-Fletcher-Goldfarb-Shanno (BFGS) (Pfrommer *et al.*, 1997), and the electronic method was ensemble density functional theory (EDFT) (Mazari *et al.*, 1997). Further convergence details per BFGS iteration are as follows: energy change per ion (dE/ion),  $2 \times 10^{-5}$  eV; electronic energy tolerance,  $10^{-8}$  eV; maximum force,  $|\text{F}|_{\text{max}} 0.05$  eV/Å; change in displacement,  $|\text{dR}| 0.002\text{Å}$ . Spin polarization was included for the Fe models.

As the aim of this work is to create illite models that are representative of layers of illite and therefore, their analysis produces data that can be compared to experimental data. The value  $|c \cdot \cos \beta|/a$  was calculated for the relaxed models as this ratio helps to determine the relative proportion of, for example, cv and tv layers (Sainz-Diaz *et al.*, 2001). All models were created and visualized using Materials Studio (Accelrys, 2012), which we also used to create simulated X-ray powder diffraction (XRPD) patterns using the Reflex module. The simulated radiation sources were  $\text{Cu-K}\alpha_1$  and  $\text{Cu-K}\alpha_2$ ; the diffractometer range was  $2\theta$  from  $5^\circ$  to  $70^\circ$ ; the temperature factor was

atomic, and the line shift Bragg-Brentano. There was no asymmetry correction applied nor any lattice strain. On the resulting simulated XRPD patterns, the major peaks up to  $30^\circ$  have been assigned their corresponding  $(h k l)$  labels. All of the  $(h k l)$ ,  $2\theta$  and  $I/I_{\max}$  (a unit-less ratio of intensities) readings up to  $30^\circ$  for all XRPD patterns shown in Section 4, can be found in the Supplementary Material.

The inclusion of Fe, and therefore a species with strongly correlated d-electrons, required a series of tests to determine the correct compensating energy in the form of a Hubbard ( $U$ ) value.

### 3.1. Determining the correct Hubbard value

Materials containing transition metals and their strongly correlated electrons can prove problematic when addressed with density functional theory, and there is no consensus on their optimum treatment. Some systems produce results closer to experiment when the d- and f-electrons are not specifically treated, whereas others produce spurious results if they are not. The Hubbard value,  $U$ , is an energy term that is added to the system such that it creates repulsion between, in this case, the d-electrons of Fe, thus reducing their strong correlations and consequently the artificially high electron density on Fe. Theoretical details can be found in Anisimov *et al.* (1997) and Mosey & Carter (2007), and an example of its implementation in Zhou *et al.* (2004). One way to determine an appropriate  $U$  value is to use experimentally measured band gaps as a guide, based on the principle that different  $U$  values produce different band gaps, hence matching a theoretical to an experimental band gap should provide a reasonable Hubbard parameter. In spite of the difference in origin between a band gap derived from DFT and that obtained experimentally, it is currently our only physical guide. For clay minerals such data are so scarce that there is an urgent need for further experimental work to be carried out on measuring the band gaps of a variety of clay minerals containing transition metals.

There are no experimental band-gap data available for Fe1Mtv, which lead to the adoption of a different approach for the calculation of an appropriate  $U$  value. This involved examining the relative shift of the valence band of the p-electrons of the tetrahedral Al; the energy-width separation of d-orbitals of Fe; the change in the band gap of Fe1Mtv, and the location of Fermi level orbitals, all with different  $U$  values. Further details of the approach, the results, and its analysis can be found in the Supplementary Material. The analysis resulted in an optimum Hubbard value of 4.5 eV, which is used throughout this study for all Fe ions.

All of the various permutations of all models listed above were allowed to fully relax, *i.e.* both the atomic positions and lattices parameters. The XRPD patterns were simulated using the relaxed models.

## 4. Results and discussion

### 4.1. Lattice parameters

#### 4.1.1. Single-layer models: tv, cv

The configurations of the relaxed, 1M-models are shown in Fig. 5 and the lattice parameters of the relaxed models are given in Table 2, together with experimental results, plus two results, “cis2” and “S7” originating from identical structures to ours, from the DFT studies of Escamilla-Roa *et al.* (2013) and Hernández-Laguna *et al.* (2006), respectively. Considering Al1Mtv, the lengths  $a$  and  $b$  and the angles  $\alpha$  and  $\gamma$  of our model agree to within 1 % of the experimental result, as expected for the GGA exchange-correlation functional, which typically exhibits under-binding and hence longer (than experimental) lattice lengths. The  $c$  length and  $\beta$  angle are 1.3 % and 1.5 %, respectively larger than the experimental values. Compared to the DFT result for structure S7,  $a$  and  $\beta$  agree within 1 %, and  $b$  and  $c$  of S7 are 1.5 % longer and 1.2 % shorter, respectively.

Similarly, for all Mg configurations  $a$  and  $b$  and  $\alpha$  and  $\gamma$  are within 1 % of the experimental values. The maximum variation of 2.9 % of  $c$  is for model Mg-c, which has a corresponding 2.3 % variation in  $\beta$ . This model is 8 meV per atom higher in energy than the lowest energy configuration (Mg-b). Model Mg-b varies in  $c$  by 2.5 % and in  $\gamma$  by 2 % from the cited experimental values.

Considering the Fe models,  $a$ ,  $b$ ,  $\alpha$ , and  $\gamma$  agreement within 1 % is repeated. The maximum variation in  $c$  is

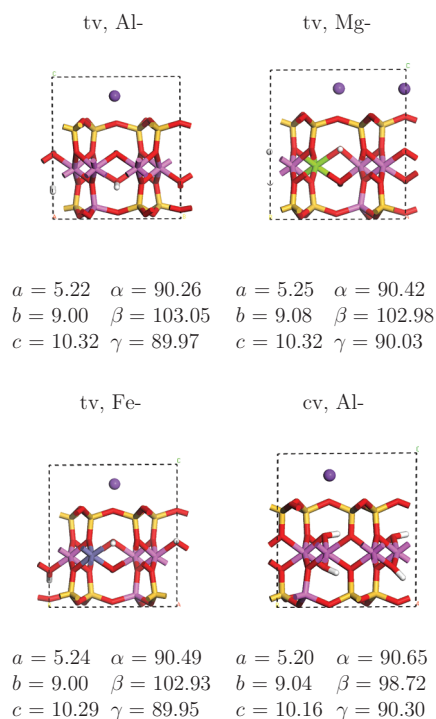


Fig. 5. Lowest-energy relaxed configurations of single unit cells.

Table 2. Lattice parameters of *1M*, single unit cells of relaxed illite models in Å and degrees. “Mg-a” refers, for example, to the unit cell of Mg-illite, with Mg in position A on Fig. 2. Final column is the energy variation from the lowest energy configuration (itself represented by “–”) and the current model. Sokolova *et al.* (1976) and Sakharov *et al.* (1990) are for *1M*-tv illite with the highest ratios of Mg and Fe in the O-sheet.

Model/Ref	<i>a</i>	<i>b</i>	<i>c</i>	$\alpha$	$\beta$	$\gamma$	$\frac{ c \cdot \cos \beta }{a}$	$\Delta E$ (meV/atom)
<i>1M</i> -tv								
Al	5.22	9	10.32	90.26	103.05	89.97	0.446	
S7	5.27	9.14	10.2	90	102.6	90	0.422	
(Środón, 1999)	5.19	8.99	10.19	90	101.52	90	0.392	
Mg-a	5.25	9.07	10.31	90.48	102.74	90.06	0.433	0.8
Mg-b	5.25	9.08	10.32	90.42	102.98	90.03	0.442	–
Mg-c	5.25	9.08	10.36	90.58	103.28	90.03	0.453	8
Mg-d	5.25	9.08	10.31	90.17	102.7	89.96	0.432	8.7
(Sokolova <i>et al.</i> , 1976)	5.21	9.01	10.07	90	100.97	90	0.368	
Fe-a	5.23	8.99	10.31	90.26	103.05	90.07	0.445	1.7
Fe-b	5.24	9	10.29	90.49	102.93	89.95	0.439	–
Fe-c	5.23	9	10.32	90.21	103.02	90.07	0.445	0.6
Fe-d	5.23	9	10.3	89.93	103.16	89.94	0.448	2.2
(Sakharov <i>et al.</i> , 1990)	5.22	9.05	10.18	90	101.24	90	0.38	
<i>1M</i> -cv								
Al	5.2	9.04	10.16	90.65	98.72	90.3	0.296	
cis2	5.26	9.11	10.1	90	98.7	90	0.29	
(Zvyagin <i>et al.</i> , 1985)	5.17	8.96	10.1	90	98.89	90	0.3	
(Drits <i>et al.</i> , 1993)	to	to	to	to	to	to	to	
(Drits <i>et al.</i> , 1995)								
(Lee, 1996)	5.2	9.01	10.16	90	99.2	90	0.312	

1.4 % and maximum  $\beta$ -angle variation is 1.9 %, the latter corresponding to the highest energy configuration.

In the case of *Al1Mcv*, the theoretical values for all lattice lengths fall within the ranges recorded experimentally and the variation of the lattice angles is a maximum of 0.7 % for  $\alpha$ , and  $\beta$  is actually lower than the experimental value by 0.2 %. Compared to the other DFT model *cis2*, there is agreement with all lattice parameters and angles within 1 %, except for *a* where that of *cis2* is 1.1 % longer.

The theoretical  $|c \cdot \cos \beta|/a$  values follow the same trends as the  $\beta$  angles, *i.e.* they are consistently higher than experiment for all tv models. For *Al1Mtv* the variation is 13.8 %; for *Mg1Mtv*, the maximum variation is 23.1 % and for *Fe1Mtv*, the minimum variation is 15.5 %. The agreement with S7 is closer, 10.2 %. For *Al1Mcv* model the variation is between 1.3 % to 5.1 % for both experiment and theory, and both theoretical model values are less than the experimental values.

#### 4.2. Sandwich models: tv, cv and mixed cv/tv

For all of the varieties of *1M*, tv-models, two minimum geometries were found, one with a  $\beta$  angle of about  $103^\circ$  and a second of about  $106^\circ$ . The permutations of Al-models with  $\beta = 106^\circ$  are lower in energy than those with  $\beta = 103^\circ$  by 0.6 meV per atom, whereas for Mg- and Fe-, the difference is less than the convergence criteria of 0.5 meV per atom, which means there are no energetic differences between them. Referring to the models shown in Fig. 6 and the data in Table 3, the models for both Al- and Mg- are examples of the relaxed permutations and are not

necessarily the lowest-energy structures because the maximum variation in energy was within the energy convergence criteria. For the Fe- models, the lowest-energy relaxed models are given, together with the maximum variation of energy per atom displayed by permutations other than those shown. There are two values recorded, corresponding to two different spin states. The lower values of 0.6 and 0.8 represent the maximum energy difference between permutations of the same, lower spin state, and the higher values (4.7, 5.4) that between different, higher spin states. The lower spin state corresponds to  $\text{Fe}^{3+}$ , the higher to  $\text{Fe}^{2+}$ . The higher spin states appeared only twice, and these were random results, implying that it is difficult to control the oxidation state of Fe within clay minerals. Perhaps this is not merely a modelling phenomenon but occurs naturally too, that is, the  $\text{Fe}^{2+}$  state is not stable in nature, hence it usually constitutes a lower percentage of the overall octahedral Fe content.

For all Al-cv models, all relaxed permutations are shown in Fig. 7 and Table 3, because the energy differences between them are greater than the energy convergence criteria and there are also differences in lattice parameters.

All lattice lengths for the tv models lie within 1 % of the quoted experimental values (comparison made with double the experimental *c*-lengths), as do the angles  $\alpha$  and  $\gamma$  apart from the  $\alpha$  angle of Fe ( $91.00^\circ$ ), which is 1.1 % larger than the experimental value. The main variation lies in  $\beta$  for all tv models. Considering the models with a  $\beta$  angle closer to  $103^\circ$  than  $106^\circ$ , then for Al, there is a 1.2 % variation, for Mg, 1.33 %, and for Fe, 1.5 %. For the  $106^\circ$  models, this becomes 4.7 % for Al and Mg and 5.0 % for Fe.

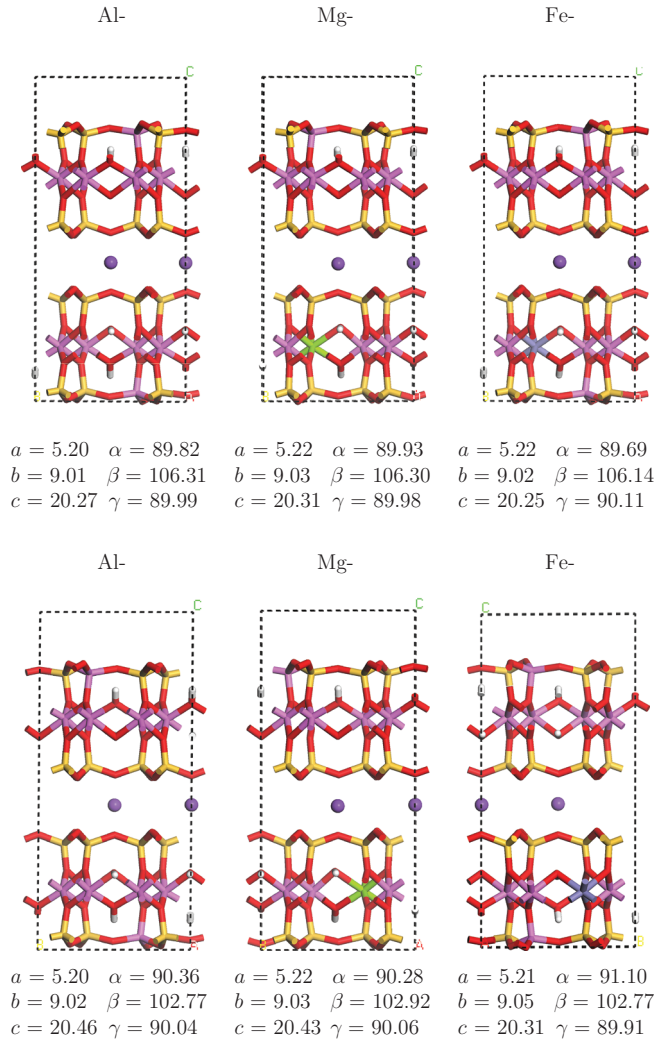


Fig. 6. Examples of relaxed configurations of tv, sandwich models.

For all permutations except the lowest energy model of Al-cv, the parameters  $a$ ,  $b$ ,  $c$ ,  $\alpha$ , and  $\gamma$  all lie within 1.0 % of the cited experimental result, as does  $\beta$  apart from the third value listed in Table 3, which varies by 1.4 %. The lowest-energy model agrees with experiment to within 1 % in  $a$ ,  $b$ ,  $\alpha$ , and  $\gamma$ , and varies by 2.4 % in  $c$  and by 5.0 % in  $\beta$ .

The experimental values cited for the mixed, cv/tv illite are for interstratified layers, hence must have an averaged  $c$  length, which is less than half that of the theoretical models. For the purposes of comparison, assume that the experimental value of  $c$  is double that given, *i.e.* 20.24 Å. The maximum difference in energy between the permutations of mixed, cv/tv illite is 0.12 meV per atom, which is within the energy convergence criteria previously stated, hence only the highest and lowest in energy are shown. Both models agree with experimental values of  $a$ ,  $b$ , and  $\gamma$  within 1 % ( $\alpha$  of Mg-c also falls within this expected error bound). Both models have  $c$  lengths 1.6 % greater than experiment and their  $\beta$  angles are 1.8 % smaller than experiment. Unusually,  $\alpha$  of the lowest energy model differs by 3.2 % from the experimental value.

The variation in  $|c \cdot \cos \beta|/a$  for tv, Al- and Mg- lies between about 11 % for the 103° models and 40 % for the 106° models; for Fe- these values are 13 % and 43 % respectively. For cv, Al- models, the variation of the  $|c \cdot \cos \beta|/a$  value is about 8 % for all but the lowest-energy model, where it is 50 %. For mixed, cv/tv Al-, the variation is 16.5 % at the most.

There is good (within 1 %) agreement between our theoretical results and the cited experimental results for  $a$ ,  $b$ ,  $\alpha$ , and  $\gamma$  of all but two of our models. This means that the GGA exchange correlation functional is appropriate for these investigations and the disagreement with experiment is originating elsewhere. The variation for  $c$  is largest in the single-unit-cell, tv models, whereas there is agreement with experimental values for the tv sandwich models. This suggests that the absence of van der Waals forces within our models has not had a significant impact on lattice parameter predictions, since the mutual attraction of the layers for the interlayer K ions in the sandwich models effectively “corrects” the larger-than-experimental  $c$ -length of the tv, single unit cells. The lowest-energy sandwich, cv model has a  $c$ -length larger than the experimental value but the other three permutations lie within 1 % of experimental values. Both the highest- and lowest-energy models of cv/tv mixed Al/Mg also have  $c$ -lengths longer than experiment, although as previously mentioned, the cv/tv mixed experimental data must be an average from mixed ratios of cv and tv samples, so is perhaps not directly comparable. The  $\alpha$  angle of the lowest-energy model of the mixed, cv/tv model is (unusually) larger than the cited experimental value, as is  $\beta$ . Both of the lowest-energy models of the sandwich, cv varieties have lattice parameters (much) greater than those recorded from experiment, which suggests that there is no correlation between total energy and the constituents of physical samples. Therefore, when matching atomistic models to data from physical samples, it is not necessary to consider only the lowest energy permutations.

#### 4.2.1. Discussion

The largest variation between our models and experimental data is in the  $\beta$  angles for tv single and all sandwich models. As  $\beta$  is used to determine the layer displacement (in  $|c \cdot \cos \beta|/a$ ), which also depends on  $c$ , then we should consider the joint effect of the  $c$  length and  $\beta$  angle. Drits & Zviagina (2009) report that the layer displacement value differs significantly between the cis and trans configurations, where it is less than  $a/3$  for the former and greater than  $a/3$  for the latter. This is what we have found in our models, *i.e.* for the tv, single unit cells and tv, sandwich 103° models. the layer displacement is approximately  $0.4a$ , and for the cv single unit cell, sandwich and mixed cv/tv, the layer displacement is approximately  $0.3a$ . The tv, sandwich 106° models have a layer displacement of approximately  $0.5a$ , significantly higher than previously reported. Sainz-Diaz *et al.* (2001) theorized cis and trans configurations in the octahedral sheet of illite, and used these to determine cis/trans ratios of experimental data,



Table 3. Lattice parameters of sandwiches of relaxed illite models shown in Figs. 6, 7 and Al/Mg-b is the mixed cv/tv model shown in Fig. 8. Maximum energy differences between permutations of the same types are shown in the final column. Two values per Fe-model due to relaxed models with different spins, further explanation can be found in Section 4.2. (Środón, 1999) is for the highest percentage of Al and lowest Mg and Fe; (Środón, 1999) is for the percentage of Mg half that of the unit cell given in Table 2; (Sakharov *et al.*, 1990) is for the sample with a higher content of Fe than Mg; (Drits *et al.*, 1993) is for a sample of cv illite coexisting with cv-1M, tv-1M and tv-2M<sub>1</sub> illite with very low Mg and Fe content.

Model/Ref	<i>a</i>	<i>b</i>	<i>c</i>	$\alpha$	$\beta$	$\gamma$	$\frac{ c \cdot \cos \beta }{a}$	$\Delta_E$ (meV/atom)
1M-tv								
Al	5.2	9.01	20.27	89.82	106.31	89.99	0.547	0.3
Al	5.2	9.02	20.46	90.36	102.77	90.04	0.435	0.4
(Środón, 1999)	5.19	9	10.19	90	101.52	90	0.392	
Mg	5.22	9.03	20.31	89.93	106.3	89.98	0.546	0.2
Mg	5.22	9.03	20.43	90.28	102.92	90.06	0.438	0.2
(Środón, 1999)	5.2	9.01	10.21	90	101.56	90	0.393	
Fe	5.21	9.01	20.16	89.81	106.32	89.91	0.544	0.6, 4.7
Fe	5.21	9.05	20.31	91	102.77	89.91	0.431	0.8, 5.4
(Sakharov <i>et al.</i> , 1990)	5.22	9.05	10.18	90	101.24	90	0.38	
1M-cv								
Al	5.2	9.01	20.01	89.44	100.21	90.1	0.343	0.7
Al	5.19	9.02	19.99	89.26	100.09	90.01	0.337	1
Al	5.2	9.02	19.79	90.03	104.2	89.99	0.467	–
Al	5.2	9.01	20.07	89.41	100.58	90.08	0.354	0.6
(Drits <i>et al.</i> , 1993)	5.19	9	10.14	90	99.18	90	0.311	
1M-cv/tv								
Al/Mg-b	5.21	9.04	20.39	92.89	98.47	90.05	0.288	–
Al/Mg-c	5.22	9.03	20.4	89.24	98.53	89.98	0.3	0.12
(Gavrilov & Tsipursky, 1988)	5.19	8.99	10.12	90	100.3	90	0.345	

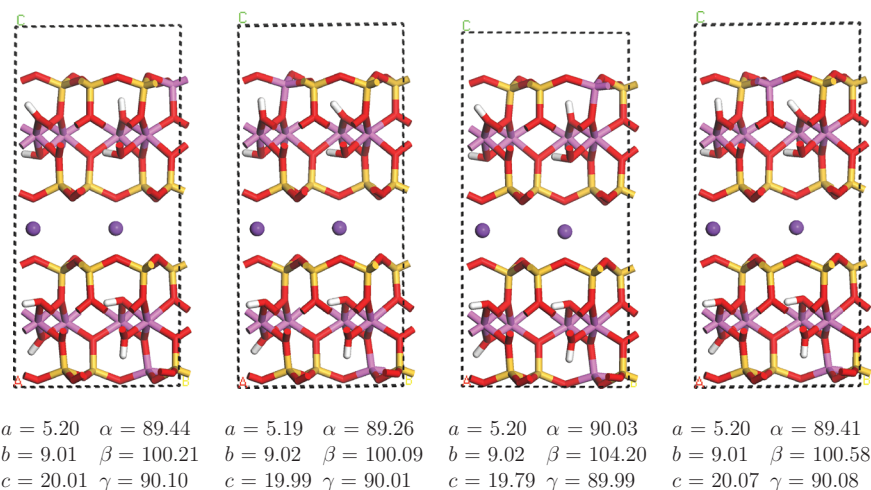


Fig. 7. Relaxed configurations of cv, sandwich Al-illite.

adjusted by their calculated layer displacement ratios. For one sample with experimental parameters (Drits *et al.*, 1993; 1998) of  $a = 5.18$ ,  $b = 8.97$ ,  $c = 10.05$ ,  $\alpha = \gamma = 90.0^\circ$ ,  $\beta = 100.4^\circ$ , Sainz-Diaz *et al.* (2001) calculated a trans-layer proportion of 0.78 with  $a = 5.23$ ,  $b = 8.90$ ,  $c = 10.20$ ,  $\alpha = \gamma = 90.0^\circ$ ,  $\beta = 105.7^\circ$ , and for a second sample with experimental parameters of  $a = 5.18$ ,  $b = 8.98$ ,  $c = 10.05$ ,  $\alpha = \gamma = 90.0^\circ$ ,  $\beta = 101.4^\circ$ , they calculated a trans-layer proportion of 0.61 with  $a = 5.23$ ,  $b = 8.92$ ,  $c = 10.10$ ,  $\alpha = \gamma = 90.0^\circ$ ,  $\beta = 105.0^\circ$ . The adjusted  $\beta$  values for the experimental samples are  $101.7^\circ$  and  $103.6^\circ$ , respectively. Sainz-Diaz *et al.*'s work provides

evidence that our  $106^\circ$  models are feasible (they are now within 1% of the  $\beta$  angle of Sainz-Diaz' theoretical,  $105.7^\circ$  and  $105^\circ$  models). Their work also shows that the proportion of cis to trans layers in an illite sample controls the experimentally measured parameters, and that this effect on  $\beta$  is random – the values could be higher or lower with a higher proportion of trans and likewise with cis. The question arises, how all of this should be interpreted. One possibility is that the  $106^\circ$  tv, sandwich models could exist in nature and their parameters have been obscured by the different ratios of cis to trans layers. It is also possible that the tv, sandwich models are constrained in

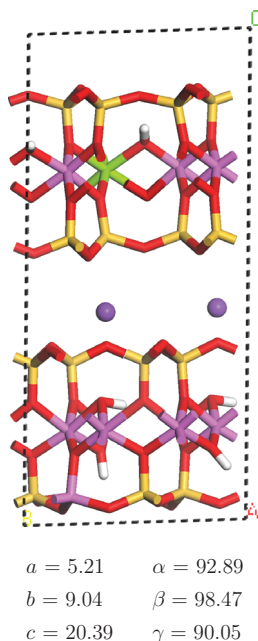


Fig. 8. Lowest-energy relaxed configuration of cv/tv Al/Mg-illite.

their natural environment by the presence of cv layers, and do not commonly exist as  $106^\circ$  structures.

It is interesting that the closest agreement with the experimental data is given by the all-Al, cv, single unit cell model, and its parameters are less than the experimental values. So, if the cv models are less than experiment and the tv, greater, then a combination could match experiment exactly, as Sainz-Diaz's work shows. It is also interesting that the cv single-unit and sandwich models (apart from cv sandwich, lowest energy) and the mixed cv/tv model all have a layer displacement ratio of approximately  $0.3a$ . The implication is that the cv layers have a constraining effect on the tv layers, and that the experimentally measured parameters (with  $\beta$  being the main focus here) are a result of an interplay between  $\beta$  of the constituent cis and trans models together with the proportion of cis and trans layers.

There is sufficient agreement between the lattice parameters of the cited experimental and theoretical work, and our atomistic models to conclude that the theoretical models we present here are valid representations of structures found within the 1M-illite series. There is no clear evidence to say that any of them could not exist in Nature.

One final thing to note is that the lattice parameters do not depend on the substituted octahedral cation, in contrast to the findings of Drits & Zviagina (2009), who found that the layer displacement ratio depends on the number of substituted  $M^{2+}$  octahedral (M) cations, increasing linearly with increasing substitution. We have probably not revealed this trend because we have only one substituted octahedral cation per model.

### 4.3. Vacancy site and general interatomic measurements

Drits *et al.* (2006) simulated tv and cv 1M-structures of dioctahedral 2:1 micas with the cation composition  $K_{0.74}Na_{0.03}Mg_{0.01}(Al_{1.87}Fe^{3+}_{0.04}Mg_{0.09})(Si_{3.28}Al_{0.72})$ , using a code developed by Smoliar-Zviagina (1993), who created an algorithm to simulate atomic coordinates from cation composition and unit-cell parameters. The algorithm predicated on the relationships found between structural parameters and chemical constituents of published compositions of dioctahedral 1M- and  $2M_1$ -micas. In our study, we examine the internal lengths of the edges encompassing a vacant site in the octahedral sheets, and internal bond-lengths of a selection of our models and compare them with those simulated by Drits *et al.* (2006). The relevant vacant-site lengths are illustrated in Fig. 9 and presented in Table 4. The largest variation between our data and that of Drits *et al.* (2006) occurs for the 1Mtv (single-layer) models for Mg1Mtv at 5.5 % and for the sandwiches, the maximum variations occur for Fe1Mtv( $103^\circ$ ) at 6.8 %; Mg1Mtv( $103^\circ$ ) at 5.5 % and for the bottom, tv-layer of the mixed Al/Mg model at 5.1 %. There is excellent agreement between all types of 1Mcv models presented, with a maximum variation of 3 % for each, but mostly the variation is less than 1 %.

Tables 5 and 6 compare selected interatomic distances from a range of our tv and cv models with those recorded by Drits *et al.* (2006), who calculated mean interatomic distances based on an equation relating mean tetrahedral cation-oxygen distances to the type of cation. Consequently, we have calculated mean distances based on the ratio of Si to Al tetrahedra, and similarly for the octahedra. Scrutinizing Table 5 reveals the tv, Si tetrahedra to be slightly smaller than the Al tetrahedra, but when an average is taken based on ratios found in unit cells or sandwiches, all mean tetrahedral measurements match those of Drits *et al.* (2006) very closely, with a maximum deviation of 1.1 %. Considering the octahedra, there are individual variations in their dimensions depending on

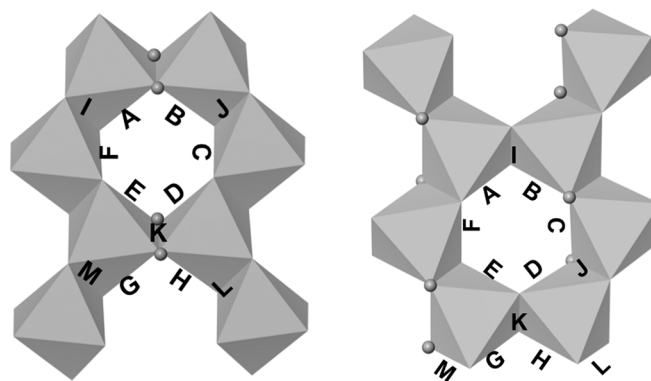


Fig. 9. Octahedral labels relevant to Table 4 reproducing the format of Drits *et al.* (2006) for fragments of octahedral sheets of tv (left) and cv (right), projected on the  $a$ - $b$  plane. Balls represent O-H bonds.

Table 4. Lengths (in Å) of sides of octahedral edges surrounding hexagonal vacancy in octahedral sheets (as labelled in Fig. 9) of a sample of the relaxed models. I-I, Alcv(104°) is one of the cv sandwiches shown in Fig.7; Al/Mg1M/tv and Al/Mg1M/cv are the tv and cv layers respectively, in the mixed Al/Mg1Mcv/tv model.

MODEL	A	B	C	D	E	F	G	H	I	J	K	L	M
Drits tv	2.86	2.86	2.93	2.86	2.86	2.93	2.86	2.86	2.47	2.47	2.39	2.47	2.47
Al1Mtv	2.87	2.86	2.95	2.89	2.89	3	2.87	2.86	2.45	2.43	2.36	2.43	2.45
Mg1Mtv	2.8	2.81	3.09	2.78	2.81	3	2.8	2.81	2.46	2.6	2.44	2.6	2.46
Fe1Mtv	2.87	2.81	2.93	2.85	2.89	3	2.87	2.81	2.46	2.48	2.37	2.48	2.46
Al(106°)	2.85	2.85	2.95	2.85	2.85	3	2.85	2.85	2.46	2.45	2.39	2.45	2.46
Al(103°)	2.84	2.84	2.99	2.85	2.85	2.94	2.84	2.84	2.45	2.46	2.39	2.46	2.45
Mg(106°)	2.79	2.8	3.08	2.78	2.8	2.95	2.79	2.8	2.48	2.59	2.45	2.59	2.48
Mg(103°)	2.79	2.79	2.95	2.79	2.8	3.09	2.79	2.79	2.61	2.48	2.45	2.48	2.61
Fe(106°)	2.85	2.82	2.95	2.82	2.85	2.99	2.85	2.82	2.46	2.48	2.4	2.48	2.46
Fe(103°)	2.84	2.79	2.96	2.85	2.79	3.13	2.84	2.79	2.52	2.48	2.41	2.48	2.52
Al/Mg1Mtv	2.79	2.78	3.1	2.81	2.77	2.93	2.79	2.78	2.5	2.6	2.45	2.6	2.5
Drits cv	2.9	2.87	2.8	2.87	2.9	2.9	2.9	2.87	2.46	2.42	2.46	2.42	2.42
Al1Mcv	2.98	2.89	2.83	2.94	2.9	2.88	2.98	2.89	2.45	2.39	2.45	2.42	2.4
I-I, Alcv(104°)	2.99	2.85	2.78	2.9	2.88	2.99	2.99	2.85	2.46	2.4	2.46	2.47	2.4
Al/Mg1Mcv	2.99	2.84	2.78	2.91	2.86	2.99	2.99	2.84	2.46	2.4	2.46	2.48	2.39

Table 5. Examples of mean interatomic distances (dashed-lines and bold type) in 1M tv models compared to those simulated by Drits *et al.* (2006). T/O refers to the type of polyhedron in the tetrahedral and octahedral sheets respectively, and Mean T 14:2, O 7:1 refers to the tetrahedral ratio of 14 Si to 2 Al, and octahedral ratio of 7 Al to 1 Fe respectively, for example. Numbered "O" on header-figures refer to oxygens.

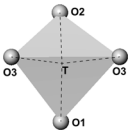
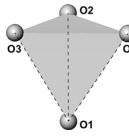
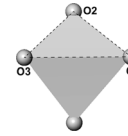
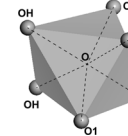
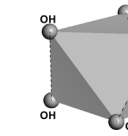
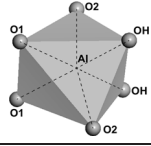
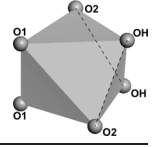
Model T/O					
<b>Drits</b>	<b>1.64</b>	<b>2.7</b>	<b>2.65</b>	<b>1.93</b>	<b>2.43</b>
Al1Mtv Si/Al	1.62	2.68	2.62	1.93	2.42
Al1Mtv Al/-	1.74	2.86	2.84	-	-
<b>Mean T 7:1, O 4:0</b>	<b>1.64</b>	<b>2.7</b>	<b>2.65</b>	<b>1.93</b>	<b>2.43</b>
Mg1Mtv Si/Al	1.63	2.69	2.63	1.92	2.47
Mg1Mtv Al/Mg	1.75	2.9	2.8	2.1	2.59
<b>Mean T 7:1, O 3:1</b>	<b>1.65</b>	<b>2.72</b>	<b>2.65</b>	<b>1.97</b>	<b>2.5</b>
Fe1Mtv Si/Al	1.62	2.68	2.61	1.93	2.42
Fe1Mtv Al/Fe	1.74	2.86	2.83	1.97	2.49
<b>Mean T 7:1, O 3:1</b>	<b>1.64</b>	<b>2.7</b>	<b>2.64</b>	<b>1.94</b>	<b>2.44</b>
Al(106°) Si/Al	1.63	2.7	2.6	1.94	2.44
Al(106°) Al/-	1.75	2.8	2.91	-	-
<b>Mean T 14:2, O 8:0</b>	<b>1.65</b>	<b>2.71</b>	<b>2.64</b>	<b>1.94</b>	<b>2.44</b>
Al(103°) Si/Al	1.63	2.71	2.61	1.94	2.44
Al(103°) Al/-	1.75	2.86	2.89	-	-
<b>Mean T 14:2, O 8:0</b>	<b>1.65</b>	<b>2.73</b>	<b>2.65</b>	<b>1.94</b>	<b>2.44</b>
Mg(106°) Si/Al	1.63	2.7	2.61	1.94	2.43
Mg(106°) Al/Mg	1.75	2.81	2.9	2.08	2.58
<b>Mean T 15:1, O 7:1</b>	<b>1.64</b>	<b>2.71</b>	<b>2.63</b>	<b>1.96</b>	<b>2.45</b>
Mg(103°) Si/Al	1.63	2.7	2.61	1.93	2.43
Mg(103°) Al/Mg	1.75	2.81	2.89	2.09	2.58
<b>Mean T 15:1, O 7:1</b>	<b>1.64</b>	<b>2.71</b>	<b>2.63</b>	<b>1.95</b>	<b>2.45</b>
Fe(106°) Si/Al	1.63	2.65	2.67	1.94	2.46
Fe(106°) Al/Fe	1.75	2.8	2.91	1.97	2.48
<b>Mean T 14:2, O 7:1</b>	<b>1.65</b>	<b>2.67</b>	<b>2.7</b>	<b>1.94</b>	<b>2.46</b>
Fe(103°) Si/Al	1.63	2.65	2.67	1.93	2.48
Fe(103°) Al/Fe	1.75	2.81	2.89	2.03	2.52
<b>Mean T 14:2, O 7:1</b>	<b>1.65</b>	<b>2.67</b>	<b>2.7</b>	<b>1.94</b>	<b>2.49</b>
Al/Mg(tv) Si/Al	1.62	2.67	2.63	1.93	2.4
Al/Mg(tv) -/Mg	-	-	-	2.09	2.58
<b>Mean T 8:0, O 3:1</b>	<b>1.62</b>	<b>2.67</b>	<b>2.63</b>	<b>1.97</b>	<b>2.45</b>

Table 6. Examples of mean interatomic distances (dashed-lines) in 1M cv models compared to those simulated by Drits *et al.* (2006).

Model		
Drits cv	1.93	2.42
Al1Mcv	1.93	2.41
I-I, Alcv(104°)	1.93	2.43
Al/Mg(cv)	1.94	2.44

whether they are Al, Mg or Fe, that is, Al and Fe octahedra are very similar in dimensions and Mg are slightly larger. However, averaging these measurements based on their ratios for unit cell and sandwich models, reveals a very close match to those of Drits *et al.* (2006), with a maximum variation of 2.9 % for the unit cell, Mg1Mtv model.

Table 6 shows a selection of octahedral measurements of the cv-models that are all in excellent agreement with those of Drits *et al.* (2006).

#### 4.3.1. Discussion

Most of the variation between our results and those of Drits *et al.* (2006) for both the vacancy site and interatomic distances occurs for the 1Mtv models containing Mg. This is not surprising given that the average (of ionic and covalent) radii increases from Al through Fe to Mg, and Fe is closer to Al than to Mg. There are no significant differences in maximum variations between the unit cells and sandwiches. The overall excellent agreement with Drits *et al.* (2006) seen for the cv models is not that surprising given that their coordinates were used as the template for our cv models, but it does prove that DFT is a suitable and reliable method for investigating these clay mineral structures. The generally excellent agreement between the data of Drits *et al.* (2006) and the selected vacancy site and interatomic measurements instils confidence that both the tetrahedral and octahedral sheet compositions and conformations of all of our models are representative of physical samples of dioctahedral, 2:1 mica. Focussing next on the K ion and its locale should reveal more about the validity of our models being representative of physical samples of illite I and I-I layers found within shale.

#### 4.4. K–O distances, location of K ion and basal surface corrugations

The average distance between the K ions and the basal surface oxygens can be found in Table 7. Considering the tv and cv, single unit cells, the K–O distances are all very similar, varying by about 0.6 % apart from in the Mg-models where the K–O lengths are between 1.6 to 3.5 % longer than those in Al- and Fe-. All of these K–O distances vary from the cited values by between 9.4 to 12.8 %.

Table 7. Average K–O distances in 1M models. “Top” refers to the layer above the K ion and “Bottom” to the layer below, which are used interchangeably with “upper” and “lower” respectively, in the main text. For the tv, sandwich models the (106°) and (103°) refer to the two different sets of models shown in Fig. 6.

Model	K1		K2	
	Top	Bottom	Top	Bottom
tv, single layer				
Al	–	3.15	–	–
Mg	–	3.25	–	3.19
Fe	–	3.16	–	–
(Drits <i>et al.</i> , 2006)	mean 2.88			
cv single layer				
Al	–	3.14	–	–
(Drits <i>et al.</i> , 2006)	mean 2.88			
tv, sandwiches				
Al(106°)	3.09	3.1	3.09	3.09
Al(103°)	3.08	3.09	3.1	3.09
Mg(106°)	3.15	3.07	3.12	3.06
Mg(103°)	3.12	3.06	3.15	3.07
Fe(106°)	3.1	3.09	3.1	3.1
Fe(103°)	3.1	3.09	3.11	3.1
cv, sandwiches				
Al	3.07	3.1	3.09	3.08
mixed, cv/tv				
Al/Mg	2.86	2.97	2.84	2.98

The variation between the K–O distances of the tv, sandwich, 106° and 103° models of Al- and Fe- is about 1 %, and there are no discernible differences between upper and lower K–O distances. This is in contrast to the Mg- models where the upper K–O distances are either 2 or 3 % longer than the lower K–O lengths. Also, the lower K–O lengths are about 1 % shorter than the same K–O distances in Al- and Fe-, and the upper K–O lengths are about 2 % longer than the same K–O distances in Al- and Fe- models. The four K–O distances in the cv, Al- sandwich models vary by about 1 %, with no significant difference between upper and lower measurements, and with values similar to the tv, sandwich Al- and Fe- models. In the mixed cv/tv models the upper K–O lengths are approximately 5 % shorter than the lower K–O lengths.

The Al- and Fe-, tv sandwich, 106° and 103° models have K–O lengths that are between 1 to 3 % shorter than the K–O lengths of Al- and Fe- tv, single unit cells. The Mg-, tv sandwich, 106° and 103° models have K–O lengths that are between 1 to 6 % shorter than the K–O lengths in the Mg-, tv single unit cells. Similarly, the K–O lengths in the Al-, cv sandwich models are 1 to 2 % shorter than the corresponding lengths in the Al-, cv single unit cells. All K–O distances of the mixed cv/tv models are shorter than all other sandwich K–O lengths by at least 7 %.

#### 4.4.1. Discussion

The cited, mean K–O lengths of 2.88 Å have been calculated from simulated models based on samples of illite containing co-existing 1M, cv and tv types, which could explain why this length agrees better with the K–O lengths

of the mixed cv/tv model, with a maximum variation of less than 0.5 %, than with the K–O lengths of the tv and cv single unit cells. The presence in the octahedral sheet of  $Mg^{2+}$  within tv, single, sandwich and mixed models has the effect of shortening the distances between the K ions and the basal oxygens in both the layer below (and above). The presence of a second layer, for tv, cv and mixed cv/tv models also shortens the same lengths for all octahedral sheet cations. There is no significant difference between the K–O distances of cv and tv types, but there is a significant difference when a cv and a tv layer are combined to form a mixed cv/tv sandwich. In this model, there seems to be a three-fold effect on the K–O distances: the presence of Mg in the upper layer; the forming of a sandwich; and the combination of a tv and cv layer. The presence of Mg in the upper layer creates the shortest, upper K–O lengths of all the models presented here. Examining the location of  $K^+$  in the interlayer space should further illuminate the origin of these differences in K–O distances.

Representative examples of the location of  $K^+$  in the interlayer spaces can be found in Fig. 10. All of the tv models, *i.e.* Al-, Mg-, Fe-, single, sandwich,  $106^\circ$  and  $103^\circ$  all show  $K^+$  located in essentially the same location, which is within the Si–O hexagonal ring, above the two O–H groups of the octahedral sheet. The only variation is whether  $K^+$  is vertically above the two O–H groups, or, if one imagines a vertical line joining these two groups, it lies off-line. The position above the hydroxyl groups affects where  $K^+$  lies within the Si–O hexagonal ring, causing it to lie off-centre, closer to one of the hexagonal ring apices, which agrees with the calculations of Drits *et al.* (2006).

Similar to the tv models, the  $K^+$  of the (purely) cv models lies off-centre within the Si–O hexagonal ring. In contrast to the close agreement seen between the tv models

on the location of the interlayer  $K^+$ , the single and sandwich cv models show a greater difference in K location within the Si–O hexagonal ring. For the single unit cells, the two hydroxyl bonds are angled towards each other, the upper O–H more horizontal than the lower, and  $K^+$  lies directly above the centre of these “crossed” hydroxyl groups. In the sandwich models, in the lower layer the lower hydroxyl groups point downwards at a variety of near-perpendicular angles from the near-horizontal upper O–H group; in the upper layer this is reversed, *i.e.* the lower O–H groups are near-horizontal and the upper, near-perpendicular upwards. Relative to both the lower and upper layers, the K ions lie directly above the hydroxyl group pointing downwards and upwards respectively.

In the mixed cv/tv models, relative to the upper layer, the K ions lie at the centre of an  $SiO_3$  group at an apex of the Si–O hexagonal ring, three K ions alternately occupying three of the six apices. Relative to the lower layer, the location of the K ions is exactly the same as that described for the single layer, cv Al- models. The  $K^+$  occupation of the layer outside the hexagonal rings seems unusual, and suggests that in Nature, the upper layer might rotate to align its hexagonal cavities with those of the lower layer when forming mixed cv/tv, interstratified layers.

The relatively small differences in K–O distances between all models apart from the mixed cv/tv model, is due to the very similar location of  $K^+$ , off-centre within the Si–O hexagonal ring, and closely associated with the hydroxyl groups of the octahedral sheet. The larger differences in K–O distances found in the cv/tv model are due to  $K^+$  lying external to the Si–O hexagonal ring relative to the Mg-layer, and within an  $SiO_3$  “cavity”. These models imply that the position of the hydroxyl groups governs the location of  $K^+$ , and the preference is to lie within the Si–O hexagonal ring, but where this is not possible for both upper and lower layers, the  $K^+$  location might be central to an  $SiO_3$  group, although investigating whether this location is stable is beyond the scope of this study. The mixed cv/tv models give the closest agreement with calculated K–O distances and they agree well with experiment in their lattice parameters. They could also provide the clue as to where increased K occupation could occur, that is, full occupation by K of the Si–O rings only, results in a lower proportion of K than given by the average formula, *i.e.* 1  $K^+$  per  $O_{20}(OH)_4$  compared to the average formula, which has on average, 1.43  $K^+$  per  $O_{20}(OH)_4$ . One extra  $K^+$  per Si–O ring would give 1.5  $K^+$  per  $O_{20}(OH)_4$ , closer to the experimental number. However, as such occupation of  $SiO_3$  groups has not been experimentally identified, a proportional increase in K is more likely due to a corresponding increase in the number of octahedral vacancies.

Figure 11 shows a lateral view of the interlayer spaces for representative examples of the models used in this study. The tv, Al- unit cell models show the greatest degree of corrugation, with the K ions between the peaks of two V’s, one inverted and stacked on top of the other. This corrugation is characteristic of tv models as can be seen, albeit to a lesser degree than in the unit cells, in all tv models shown in Fig. 11.

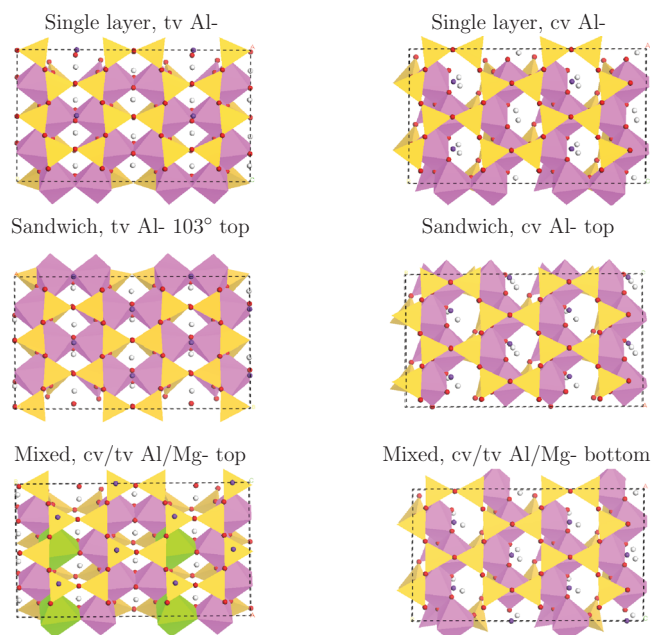


Fig. 10. Polyhedral,  $x - y$  plane views to show relative position of K ions to upper (top) and lower (bottom) layers.

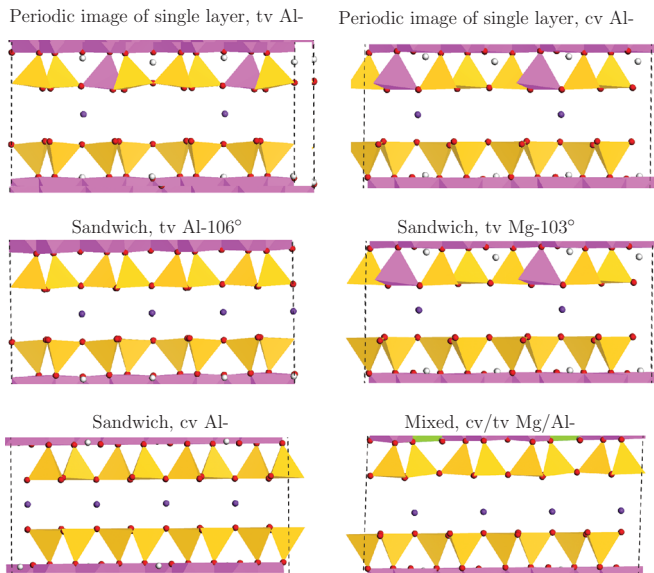


Fig. 11. Polyhedral views to show relative position of K ions to upper (top) and lower (bottom) layers.

These results agree with those of Drits *et al.* (2006). The corrugation seen in all cv models is less pronounced, and it is just about discernible that the K ions lie at the centre of two V's with the same alignment, one stacked on top of the other. These results also agree with those of Drits *et al.* (2006). The mixed cv/tv model has a mixed corrugation pattern, the lower, cv layer sharing the cv characteristics whereas the corrugation of the upper layer is translated, such that the inter-layer K ions sit to one side of the lowest-projecting, Si-O tetrahedra. This corrugation accommodates the position of  $K^+$  relative to the upper, tv, Mg-layer as previously described.

In general, the K–O distances and  $K^+$  locations within our models do not depend on whether the octahedral cation substitution is Al, Mg or Fe, although when Mg is present, there is a marginal difference, which might become more significant if the proportion of Mg substitution increases. There is also no significant difference in the  $K^+$  locations nor K–O distances between the tv and cv types. However, when tv and cv layers are conjoined, these differences are significant, and question the robustness and viability of the mixed cv/tv model. Given that the lattice parameters, vacant site and interatomic measurements of this structure all agree very well with experimental and theoretical results, it could be that a relative rotation of the two layers is necessary to align the hexagonal cavities.

#### 4.5. XRPD patterns

Characterizing the type and composition of clay minerals within samples of mudstone can be difficult enough, without the added complexity of the mudstone forming a heterogeneous matrix with organic matter within shale. Drits (2003) illustrated the general complexity involved when

identifying clay minerals within physical samples in his work focussing on the multispecimen method. This method essentially involves simulating XRD patterns of mixed-layer minerals and obtaining the best possible agreement with experimental XRD patterns; where this match occurs, the simulated and experimental structures match also. Drits' innovative technique used several treatments such as saturation by different interlayer cations, followed by glycolation and air-drying, and observing the shifts in XRD peaks and intensities. Statistical analysis then produced matching XRD patterns and hence matched simulated structures to physical samples. This brief description of Drits' work serves to illustrate how time-consuming it can be to accurately identify the composition of clay minerals, and yet this is somewhat vital if we are to make progress with illite in shale investigating the possible chemical interactions occurring within. Acknowledging that many research groups do not have the necessary facilities to emulate Drits' method, we are providing XRPD patterns of our models, which could enable characterization of the experimental structures and possibly composition of dioctahedral mica within physical samples. Comparing our simulated XRPD patterns with experimental patterns might reveal similar peaks and intensities indicative of particular characteristics, examples of which will be described shortly. All of the simulated XRPD patterns display clean spectra because they are simulated from perfectly aligned crystals, which are free of any contaminants, naturally occurring stacking faults or artifacts possibly introduced during an experiment. We have labelled the  $(h k l)$  indices up to the first ten prominent peaks on each spectrum, and have provided the  $(h k l)$  indices up to  $2\theta = 30^\circ$  for each model in the Supplementary Material. A note of caution is necessary: many polymorphs of similar composition display similar spectra, and we are providing only a very small sample of the many compositions possible, but, as we are primarily concerned with illite-series micas found within shale, which are mostly of the  $1M$ - and  $2M_1$ -type, we are narrowing the possible potential overlaps between polymorphic spectra a little.

All XRPD patterns shown in Fig. 12, to 14 display a peak between  $61^\circ$  and  $62^\circ$ , characteristic of the (060) reflection of dioctahedral phyllosilicates, which was also identified by Escamilla-Roa *et al.* (2013) in their simulated XRPD patterns of dioctahedral phyllosilicates. Zviagina *et al.* (2007) also produced simulated powder XRD patterns for a variety of dioctahedral micas, including  $1M$  tv and cv, and in agreement with their work and that of Escamilla-Roa *et al.* (2013), all of the tv models have strong (020) reflection peaks at  $20^\circ$ , whereas the cv models have strong (110) reflections peaks at  $20^\circ$ , except in one cv model of our study, *i.e.* the lowest-energy model of the Al sandwiches. This model has reflection peaks of both (020) and (110) close to  $20^\circ$ , which is perhaps due to its  $\beta$  angle of  $104^\circ$ , as this is closer to the angles of the tv models and yet its internal structure corresponds to that of the cv models. Also in agreement with these two previous studies is that the tv models have a relatively weak (or absent) reflection at  $\sim 32.5^\circ$ , whereas this is generally stronger for the cv

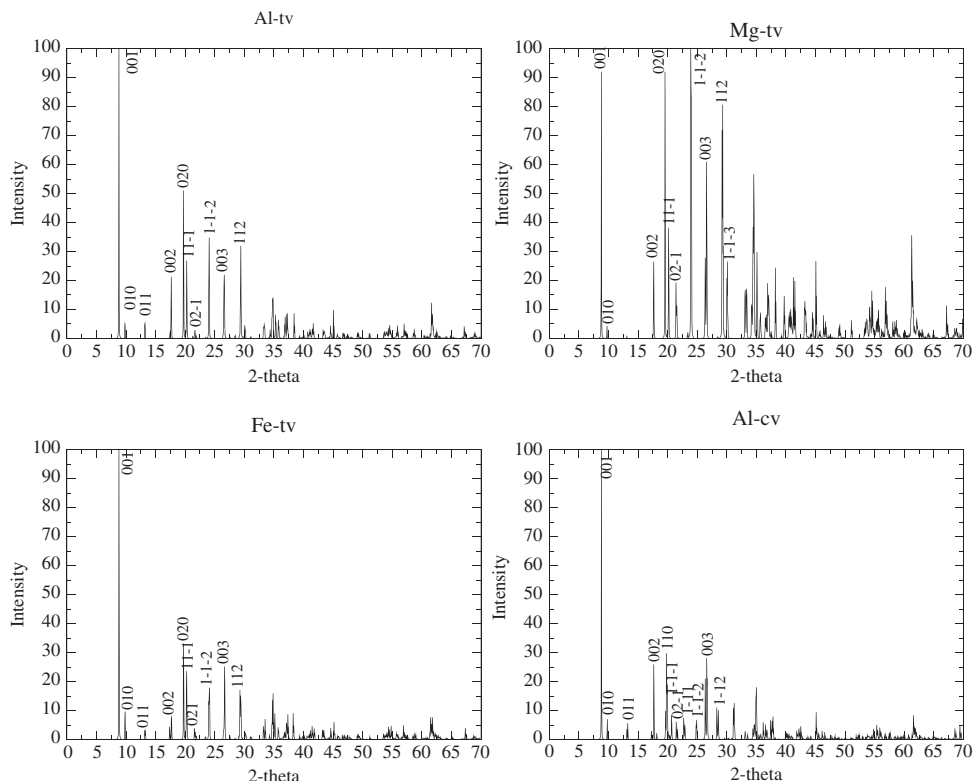


Fig. 12. Simulated XRPD patterns of tv, Al-, Mg-, Fe- and cv, Al- relaxed single layer models.

models and corresponds to a (113) reflection. Comparing between model sizes, the sandwich models (Fig. 13) have different peak intensities and  $2\theta$  angles to the single unit cells, as well as different ( $h k l$ ) reflections, although the sandwich-model group shares these reflections. For example, the (112) reflection at  $\sim 20^\circ$  is strong in the tv sandwich models but not in the single unit cells (nor the cv models). The main differences between the spectra of the  $106^\circ$  and  $103^\circ$  models is seen in some of the peak intensities.

The cv, Al- sandwich models shown in Fig. 14 show intensity and  $2\theta$  differences because the lowest-energy model has a  $\beta$  angle of  $104.20^\circ$ , whereas  $\beta$  is  $100.09^\circ$  in the highest-energy model. If these differences were experimentally identifiable in physical samples, then it would be possible to begin to identify the relative positions of the tetrahedral and octahedral sheet substitutions, as these are the source of the different lattice parameters in these cv sandwich models. Interestingly, the mixed cv/tv spectrum is qualitatively different to all others in that the first ten peaks, excluding the first, are concentrated over a smaller  $2\theta$  range and the (020) reflection peak strongest in the tv models is apparent but of lower intensity than seen in the pure tv models.

This study demonstrates qualitative agreement with the differences between tv and cv dioctahedral phyllosilicates observed in XRPD patterns by Escamilla-Roa *et al.* and Zviagina *et al.* (2007), who found their results to be consistent with those derived experimentally (Drits, 2003),

thus increasing our confidence that the models we have created can be used as examples of illite (I and I-I) layers found within gas shale.

## 5. Conclusions

We created a variety of interlayer-deficient dioctahedral mica models of the  $1M$ -illite series based on crystallographic data and average formulae, specifically representing single (I) and double (I-I) layers of illite found in gas shale. We found that the relaxed lattice parameters generally matched experimental data, and that the interatomic distances of the tetrahedral and octahedral sheets matched those of simulated micas of the same type. The differences in parameters seen in tv models with different octahedral sheet substitutions were less than those between tv and cv models. The lowest-energy theoretical model is not necessarily the best match to experimental data, and for Al- and Mg- models the permutations had no significant effect on the lattice parameters. When considering the K–O distances and location, the hydroxyl groups of the octahedral sheet determine the location of the K ion in the interlayer for all types; the octahedral cation substitutions have no effect on this position.

The XRPD data from the relaxed, theoretical models could enable experimentalists to identify some aspects of their dioctahedral mica specimens, possibly whether

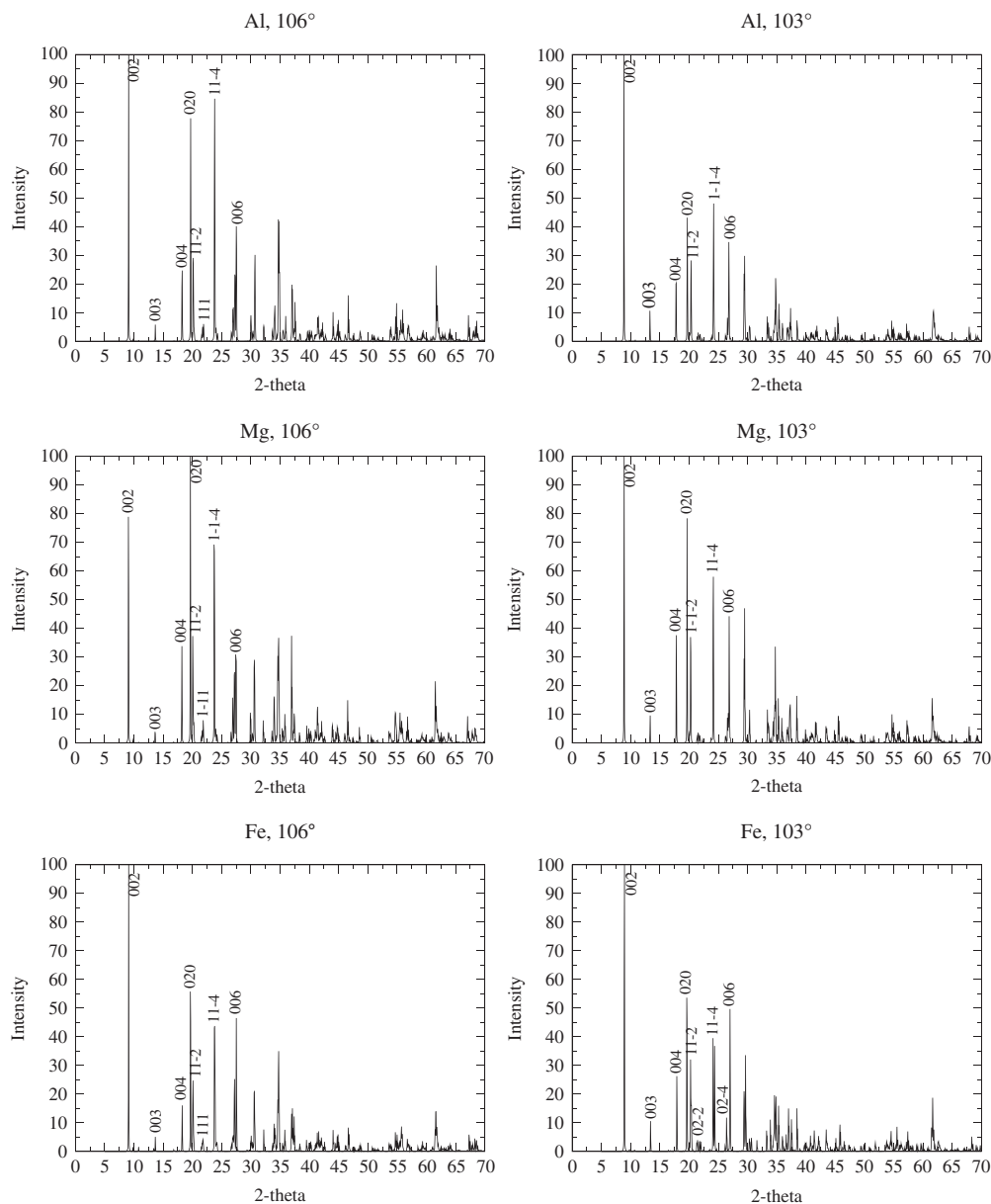


Fig. 13. Simulated XRPD patterns of tv, Al-, Mg- and Fe- of the relaxed, sandwich 106° and 103° models.

it contains tv or cv, the type of octahedral substitutions and perhaps even a particular configuration, although the clarity of the simulated XRPD patterns would be difficult if not impossible to reproduce for physical samples.

Our overall conclusion from this study is that, given the wide variety of compositions possible for individual layers of illite, every model we have produced is a valid representation of a single (I) or double layer (I-I) of illite; no strong evidence appeared in our analysis to contradict this conclusion, except for the mixed Al/Mg, cv/tv model, which requires further refinement, such as layer rotation to align the hexagonal cavities of the upper and lower layers. Our next step is to use the models and combinations of them to investigate chemical reactivity at surfaces

within gas shale, and, in the spirit of shared research, we have provided all of our relaxed models as .cif files in the Supplementary Material, so that others may also make use of them.

**Acknowledgements:** We would like to acknowledge the two anonymous reviewers for their contribution towards the final form of this manuscript. We would also like to acknowledge the high performance computing (HPC) facilities in the Center for Computational Earth and Environmental Science (CEES) at Stanford University, Dennis Michael for installing CASTEP on CEES, and the Texas Advanced Computing Center (TACC), at the University of Texas at Austin for providing HPC resources



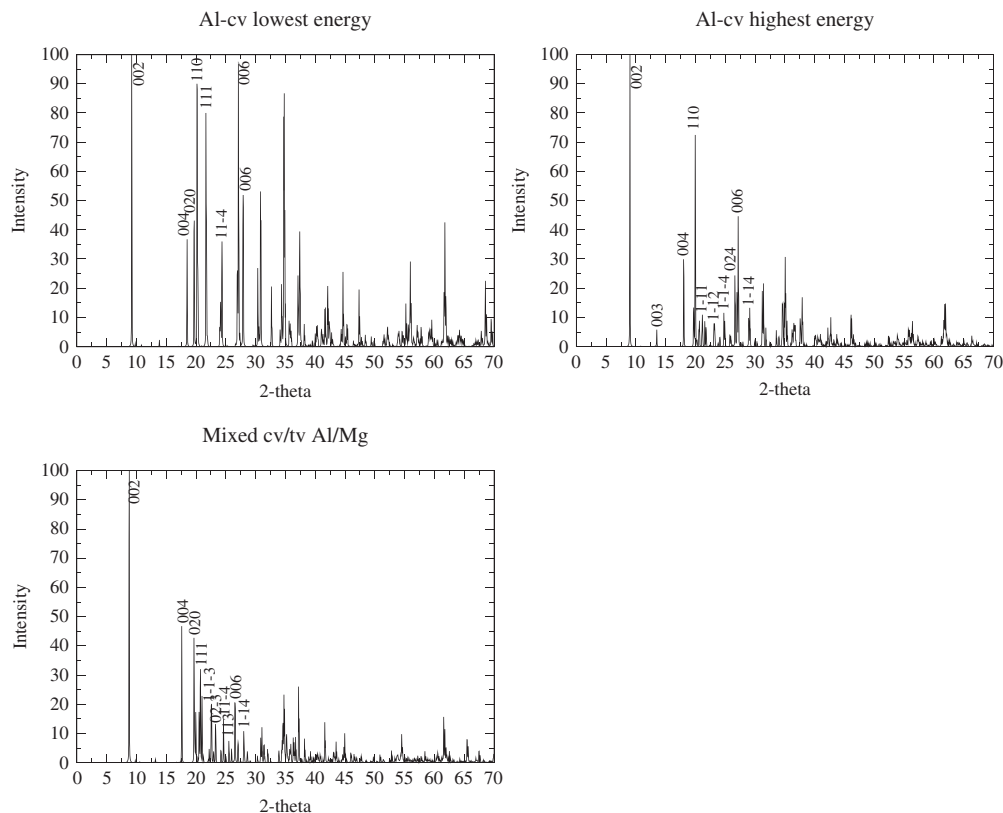


Fig. 14. Simulated XRPD patterns of 1M cv, Al- and mixed cv/tv, Mg/Al relaxed sandwich models.

that have contributed to the research results reported within this paper (<http://www.tacc.utexas.edu>). Our appreciation is also extended to the developers of the CASTEP code for their support, to Adam Jew for his helpful discussions, and finally to BP for their financial support during the course of this research.

## References

- Accelrys, (2012): Materials Studio. Modeling and Simulation Software.
- Almon, W.R. & Johns, W.D. (1975): Petroleum forming reactions: the mechanism and rate of clay catalyzed fatty acid decarboxylation. in "7th International meeting on organic geochemistry", **7**, Wiley, Chichester, 157–171.
- Anisimov, V.I., Aryasetiawan, F., Lichtenstein, A.I. (1997): First-principles calculations of the electronic structure and spectra of strongly correlated systems: the LDA +  $U$  method. *J. Phys. Condens. Matter*, **9**, 767–808.
- Bergaya, F., Theng, B.K.G., Lagaly, G. (2006): Handbook of clay science. Elsevier Ltd, Oxford.
- Clark, S.J., Segall, M.D., Pickard, C.J., Hasnip, P.J., Probert, M.I.J., Refson, K., Payne, M.C. (2005): First principles methods using CASTEP. *Z. Kristallogr.*, **220**, 567–570.
- Day-Stirrat, R.J., Loucks, R.G., Milliken, K.L., Hillier, S., van der Pluijm, B.A. (2008): Phyllosilicate orientation demonstrates early timing of compactional stabilization in calcite-cemented concretions in the Barnett Shale (Late Mississippian), Fort Worth Basin, Texas (USA). *Sedim. Geol.*, **208**, 27–35.
- Drits, V.A. (2003): Structural and chemical heterogeneity of layer silicates and clay minerals. *Clay Minerals*, **38**, 403–432.
- Drits, V.A. & Zviagina, B.B. (2009): Trans-vacant and cis-vacant 2:1 layer silicates: structural features, identification, and occurrence. *Clays Clay Minerals*, **57**, 405–415.
- Drits, V.A., Weber, F., Salyn, A.L., Tsipursky, S.I. (1993): X-ray identification of 1M illite varieties. *Clays Clay Minerals*, **28**, 185–207.
- Drits, V.A., Besson, G., Muller, F. (1995): Structural mechanism of dehydroxylation of cis-vacant 2:1 layer silicates. *Clays Clay Minerals*, **43**, 718–731.
- Drits, V.A., Lindgreen, H., Salyn, A.L., Ylagan, R.F., McCarty, D.K. (1998): Semi- quantitative determination of trans-vacant and cis-vacant 2:1 layers in illites and illite-smectites by thermal analysis and X-ray diffraction. *Am. Mineral.*, **83**, 1188–1198.
- Drits, V.A., McCarty, D.K., Zviagina, B.B. (2006): Crystal-chemical factors responsible for the distribution of octahedral cations over trans- and cis-sites in dioctahedral 2:1 layer silicates. *Clays Clay Minerals*, **54**, 131–152.
- Drits, V.A., Zviagina, B.B., McCarty, D.K., Salyn, A.L. (2010): Factors responsible for crystal-chemical variations in the solid solutions from illite to aluminoceladonite and from glauconite to celadonite. *Am. Mineral.*, **95**, 348–361.
- Escamilla-Roa, E., Hernández-Laguna, A., Sainz-Diaz, C.I. (2013): Cation arrangement in the octahedral and tetrahedral sheets of cis-vacant polymorph of dioctahedral 2:1 phyllosilicates by quantum mechanical calculations. *Am. Mineral.*, **98**, 724–435.

- Eslinger, E. & Pevear, D. (1988): Clay minerals for petroleum geologists and engineers. Society of Economic Paleontologists and Mineralogists, USA.
- Fleet, M.E. (2003): Rock-forming minerals – micas. **3A**, The Geological Society, Bath.
- Gavrilov, Y.O. & Tshipursky, S.I. (1988): Clay minerals from low- and middle- Jurassic deposits of different structural and facial zones of the central Caucasus. *Litol. Polez. Iskop.*, **6**, 57–72.
- Hernández-Laguna, H., Escamilla-Roa, E., Timón, V., Dove, M.T., Sainz-Diaz, C.I. (2006): DFT study of the cation arrangements in the octahedral and tetrahedral sheets of dioctahedral 2:1 phyllosilicates. *Phys. Chem. Minerals*, **33**, 655–666.
- Hohenberg, P. & Kohn, W. (1964): Inhomogeneous electron gas. *Phys. Rev.*, **136**, 864–871.
- Kohn, W. & Sham, L.J. (1965a): Self-consistent equations including exchange and correlation effects. *Phys. Rev.*, **140**, A1133–A1138.
- Kohn, W. & Sham, L.J. (1965b): Quantum density oscillations in an inhomogeneous electron gas. *J. Phys. Rev.*, **137**, A1697–1705.
- Lash, G.G. & Blood, D.R. (2004): Origin of shale fabric by mechanical compaction of flocculated clay: evidence from the Upper Devonian Rhinestreet shale, western New York, USA. *J. Sediment. Res.*, **74**, 110–116.
- Lausen, S.K., Lindgreen, H., Jakobsen, H.J., Nielsen, N.C. (1999): Solid-state Si-29 MAS NMR studies of illite and illite-smectite from shale. *Am. Mineral*, **84**, 1433–1438.
- Lee, M. (1996): 1M(cis) illite as an indicator of hydrothermal activities and its geological implication. in “33rd Annual Meeting of the Clay Minerals Society, Program and Abstracts”, pp. 106.
- Liming, Ji., Zhang, T., Milliken, K., Qu, J., Zhang, X. (2012): Experimental investigation of main controls to methane adsorption in clay-rich rocks. *Appl. Geochem.*, **27**, 2533–2545.
- Lindgreen, H. (1991): Elemental and structural changes in illite/smectite mixed-layer clay minerals during diagenesis in Kimmeridgian-Volgian (-Ryazanian) clays in the Central Trough, North Sea and the Norwegian-Danish Basin. *Bull. Geol. Soc. Denmark*, **39**, 1–82.
- Lindgreen, H., Jacobsen, H., Jakobsen, H.J. (1991a): Diagenetic structural transformations in North-Sea Jurassic Illite/Smectite. *Clays Clay Minerals*, **39**, 54–69.
- Lindgreen, H., Garnaes, J., Hansen, P.L., Besenbacher, F., Laegsgaard, E., Stensgaard, I., Gould, S.A.C., Hansma, P.K. (1991b): Ultrafine particles of North-Sea Illite Smectite clay-minerals investigated by STM and AFM. *Am. Mineral.*, **76**, 1218–1222.
- Mazari, N., Vanderbilt, D., Payne, M.C. (1997): Ensemble density functional theory for ab initio molecular dynamics of metals and finite-temperature insulators. *Phys. Rev. Lett.*, **79**, 1337–1340.
- Meunier, A. (2005): Clays. Springer, Berlin, Heidelberg, New York.
- Mosey, N.J. & Carter, E.A. (2007): Ab initio evaluation of Coulomb and exchange parameters for DFT + *U* calculations. *Phys. Rev. B.*, **76**, 155123–1–13.
- Nespolo, M. (2001): Perturbative theory of mica polytypism. Role of the M2 layer in the formation of inhomogeneous polytypes. *Clays Clay Minerals*, **49**, 1–23.
- Nieto, F., Mellini, M., Abad, I. (2010): The role of H<sub>3</sub>O<sup>+</sup> in the crystal structure of Illite. *Clays Clay Minerals*, **58**, 238–246.
- Payne, M.C., Teter, M.P., Allan, D.C., Arias, T.A., Joannopoulos, J.D. (1992): Iterative minimization for ab initio total-energy calculations: molecular dynamics and conjugate gradients. *Rev. Mod. Phys.*, **64**, 1045–1097.
- Perdew, J.P., Burke, K., Ernzerhof, M. (1996): Generalized gradient approximation made simple. *Phys. Rev. Lett.*, **77**, 3865–3868.
- Pfrommer, B.G., Côté, M., Louie, S., Cohen, M.L. (1997): Relaxation of crystals with the Quasi-Newton Method. *J. Comput. Phys.*, **131**, 233–240.
- Sainz-Diaz, C.I., Hernández-Laguna, A., Dove, M.T. (2001): Theoretical modelling of cis-vacant and trans-vacant configurations in the octahedral sheet of illites and smectites. *Phys. Chem. Minerals*, **28**, 322–331.
- Sakharov, B.A., Besson, G., Drits, V.A., Kameneva, M.Y., Salyn, A.L., Smoliar, B.B. (1990): X-ray study of the nature of stacking faults in the structure of glauconites. *Clay Minerals*, **25**, 419–435.
- Smoliar-Zviagina, B.B. (1993): Relationships between structural parameters and chemical composition of micas. *Clay Minerals*, **28**, 603–624.
- Sokolova, T.N., Drits, V.A., Sokolova, A.L., Stepanov, S.S. (1976): Structural and mineralogical characteristics and conditions of formation of leucophyllite from salt-bearing deposits of Inder. *Litologia and Poleznye Iskopaemye.*, **6**, 80–95.
- Środoń, J. (1999): Nature of mixed-layer clays and mechanisms of their formation and alteration. *Annu. Rev. Earth Planet. Sci.*, **27**, 19–53.
- Wilcox, J. (2012): Carbon capture. Springer, New York.
- Ylagan, R.F., Altaner, S.P., Pozzuoli, A. (2000): Reaction mechanisms of smectite illitization associated with hydrothermal alteration from Ponza Island, Italy. *Clays Clay Minerals*, **48**, 610–631.
- Zhou, F., Cococcioni, M., Marianetti, C.A., Morgan, D., Ceder, G. (2004): First-principles prediction of redox potentials in transition-metal compounds with LDA + *U*. *Phys. Rev. B.*, **70**, 235121–235128.
- Zvyagin, B.B., Rabotnov, V.T., Sidorenko, O.V., Kotelnikov, D.D. (1985): Unique mica consisting of non-centrosymmetric layers. *IZV AN SSSR Geol.*, **35**, 121–124.
- Zviagina, B.B., Sakharov, B.A., Drits, V.A. (2007): X-Ray diffraction for the identification of trans- and cis-vacant varieties of dioctahedral micas. *Clays Clay Minerals*, **55**, 467–480.
- Zöller, M. & Brockamp, O. (1997): 1M- and 2M<sub>1</sub>-illites: different minerals and not polytypes – Results from single crystal investigations at the transmission electron microscope (TEM). *Eur. J. Mineral.*, **9**, 821–827.

Received 27 May 2013

Modified version received 16 August 2013

Accepted 18 September 2013

## 7. Supplementary Material

The models in Figures 5–8 are available as .cif files in the Supplementary Material. The models are labelled according to the Figure in which they appear and alphabetical order within that Figure, which is left-to-right for each row, e.g. ‘fig. 5c.cif’ is the lowest energy, single layer, tv, Fe-illite shown in Fig. 5.